Dynamic response of sloshing pressure sensors

Schreier, Sebastian; Cornel, Wout; Poelma, Christian

Publication date
2019

Document Version
Final published version

Published in
Proceedings of the 29th International Ocean and Polar Engineering Conference (ISOPE 2019)

Proceedings of the Twenty-ninth (2019) International Ocean and Polar Engineering Conference **www.isope.org**
Honolulu, Hawaii, USA, June 16-21, 2019

ISBN 978-1 880653 85-2; ISSN 1098-6189

Dynamic Response of Sloshing Pressure Sensors

Sebastian Schreier, Wouter A. Cornel, Christian Poelma
Faculty 3mE, Delft University of Technology
Delft, The Netherlands

ABSTRACT

The dynamic response of pressure sensors for model tests of sloshing impacts is paramount to recording these highly dynamic events. In this study, we investigated the dynamic behavior of the new pressure sensors presented at ISOPE 2018 (Schreier and Poelma, 2018), which increased the spatial resolution of sloshing pressure measurements by a factor of 5 compared to common sloshing pressure sensor arrangements. Wet drop tests were conducted and the resulting pressure signals were compared to theoretical results of the Wagner solution. For peak pressures over the full measurement range of the sensors, the rise time was found to be less than 0.25 ms, which was close to the theoretical minimum rise time of the generated pressures. Furthermore, the pressure sensors were found to have low sensitivity to accelerations. The results of this study indicated that these new pressure sensors were applicable for sloshing investigations.

KEY WORDS: Sloshing Model Tests; Drop Tests; Pressure Sensors; Dynamic Response; Sensor Development

INTRODUCTION

Sloshing impacts are highly dynamic events with a duration of only several milliseconds (Kim et al., 2015). Within this timespan, the pressure caused by the liquid hitting a structure reaches its peak and then drops again to much smaller values. Furthermore, depending on the shape of the free liquid surface directly prior to the impact, sloshing impact pressures can vary greatly in space. Therefore, pressure sensors are required that allow for high spatial and temporal resolution for experimental investigations into the spatial and temporal variability of sloshing impact pressures. In 2018, Schreier and Poelma introduced new sloshing pressure sensors based on MEMS technology. With in-plane dimension of 1.7 mm by 1.7 mm, these sensors increase spatial resolution of sloshing pressure measurements by a factor of 5 compared to the pressure sensor arrangements commonly in use (Ahn et al., 2013, Loysel et al., 2012 & 2013). The previous study demonstrated the good static response of the sensors.

In this study, we investigated the dynamic response of those pressure sensors to determine the extent of the applicability of these new sensors to highly dynamic events such as sloshing impacts. Wet drop tests of wedges with different deadrise angle have been conducted before e.g. by Chuang (1966), Truong et al. (2010), Nikfarjam et al. (2017), Shin et al. (2018), and have shown good repeatability of the generated peak pressures (Kim et al., 2016). Therefore, we opted for wet drop tests with individual pressure sensors as well as arrays of 5 pressure sensors in one line mounted on a wedge impactor with 10° deadrise angle. Furthermore, we conducted dry acceleration tests with a single sensor and a hammer test of the drop test facility. The data assessment focused on peak pressure, rise time, and sensitivity to accelerations. For the peak pressures, theoretical results according to Wagner (1932) as well as Okada and Sumi (2000) were employed as reference. Rise time was compared to the findings of Kim et al. (2015) as well as the recommendations of Razzak et al. (2013).

MEASUREMENT EQUIPMENT AND TEST SETUP

Pressure Sensors and Accelerometer

The pressure sensing devices used in this study were EPCOS C32 industrial with absolute pressure range of 160 kPa, in-plane dimensions of 1.7 mm by 1.7 mm, and a vacuum reference cavity at their back. These piezoresistive semiconductor dies were based on the working principle of a Wheatstone bridge. Typical sensitivity of these devices was given as 0.14 (mV/V)/kPa with a nominal excitation voltage of 5 V. Non-linearity was specified as 0.3% of the measuring range (EPCOS, 2009).

To enable wiring the sensors, the sensing devices were mounted in printed circuit boards as shown in Figs. 1 and 2. Sensing devices were inserted into holes milled into the circuit boards to achieve flush underside and minimize cavity volume on the pressure ports. The sensing devices were glued into place by UV-hardening glue. Two different sensor arrays were used in this study: the type PSC1_5s with 5 sensors in a row with a spacing of 3.2 mm center to center and the type PSC1_1 comprising a single sensor.

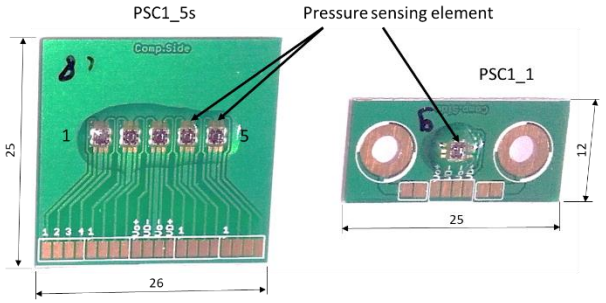

Fig. 1. Printed circuit boards with small pressure sensors. Left: type PSC1_5s with array of 5 sensors; right: type PSC1_1 comprising single sensor. Picture shows dry side of the sensors. Dimensions are given in millimeters.

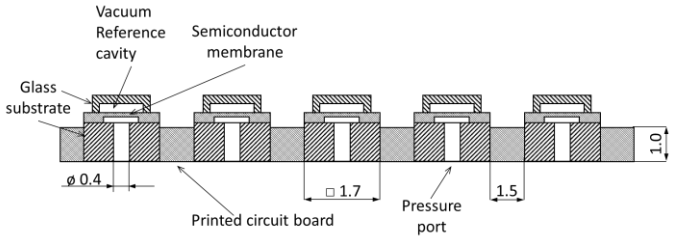

Fig. 2. Schematic side view section of the pressure sensors in the printed circuit board. Dimensions are given in millimeters. Sketch not to scale.

Furthermore, one PCB Piezotronics piezoelectric accelerometer of type M353B18 with a range of 4905 m/s^2 and a sensitivity of 1.02 mV/(m/s^2) was employed in combination with a signal conditioner M482A22 of the same manufacturer. The resonant frequency of this sensor was specified by the manufacturer as ≥ 70 kHz (PCB Piezotronics, 2011).

Data Acquisition System and High-speed Camera

The data acquisition system comprised equipment from National Instruments and was based on an NI PXIe-1078 chassis with an NI PXIe-8840 Quad Core controller. Module NI PXIe-4331 bridge amplifier with 8 channels of 24 bit resolution was used for recording the pressure data. The bridge excitation voltage was set to 2.5 V DC and input range to ± 25 mV/V. This module contains an input filter with a passband up to $0.45 \cdot f_s$ for sampling rates $f_s > 25.6$ kHz (National Instruments Corp., 2010). The acceleration signal was recorded by analogue input module NI PXI-6143 with 16 bit resolution and input range of ± 5 V. The sampling rate was set to 100 kHz for all channels and sampling was synchronized by sharing a common time base and using an internal trigger signal between the modules.

The wet drop tests were further recorded by a high-speed camera LaVision Imager Pro HS 4M, CMOS with 36 GB of memory and 16 bit grayscale resolution. The image size was selected as 1632 x 816 pixels at a frame rate of 3000 fps. The aperture was set to 5.6 and the exposure time was 250 microseconds.

Test Setup

Dry Acceleration Test

For the dry acceleration tests, the accelerometer was attached to the dry side of one of the single PSC1_1 sensors, labelled Pxx, by means of a sticky wax as shown in Fig. 3. The accelerometer was positioned on the protective glue and directly above the pressure sensor. With this orientation, an acceleration of the pressure sensor towards the accelerometer, i.e. towards the right in Fig. 3, was recorded as positive. This sensor assembly was simply held up in air by the cables and excitation was provided by ticking the pressure side of the circuit board on the short edge in the foreground in Fig. 3 with a fingernail.

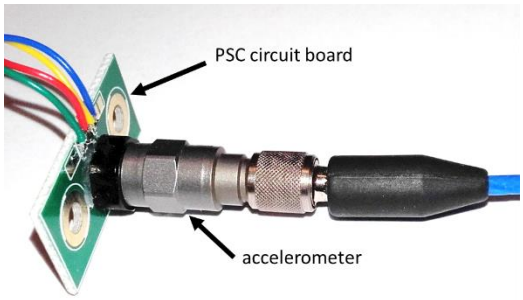

Fig. 3. Test setup for dry acceleration tests.

Wet Drop Test

For the wet drop tests, a symmetric impactor wedge with 10° deadrise angle and dimensions of 200 mm in length and 95 mm in width was built from Perspex material of 20 mm thickness. On one side of the sloping bottom plates, three single pressure sensors of type PSC1_1 were mounted, and on the other side, the two sensor arrays of type PSC1_5s were placed. The circuit boards with the pressure sensors were inserted into recesses milled into the bottom plates. The pressure side of the circuit boards was aligned flush with the lower face of the bottom plates and the recesses were filled by molten paraffin wax. Excess paraffin was scraped of carefully after the wax had set. Paraffin wax was chosen because of its low melting point within the allowable temperature range of the pressure sensors and to be able to remove the pressure sensors from the impactor wedge without causing damage. Fig. 4 presents the bottom view of the impactor wedge with the pressure sensors installed. The sensors were labelled P01 through P13 as identified in Fig. 4.

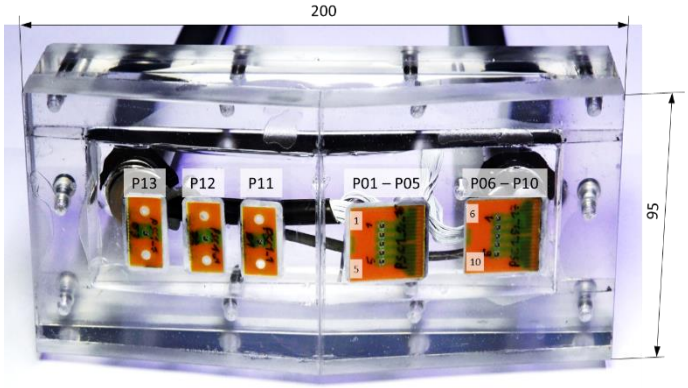

Fig. 4. Pressure sensors mounted on bottom of impactor wedge. Dimensions are given in millimeters.

In transverse direction, the pressure sensors were centered on the longitudinal center plane of the wedge. Their position in longitudinal direction is summarized in Tab. 1, measured along the sloping bottom w.r.t. to the apex.

Tab. 1. Sensor position along bottom of wedge w.r.t. to apex (in mm).

P13	P12	P11	P01-P05	P06-P10
-63	-41	-22	23	64

The drop test facility is shown in Fig. 5. The frame was built from X95 aluminum profiles and supported two vertical cylindrical guiderails. The falling crosshead was attached to the guiderails by linear ball bearings on each side. A vertical aluminum bar with holes at 20 mm spacing was mounted to the support frame and ensured reproducible drop height. A locking pin inserted through one of the holes in the aluminum bar into a matching hole in the crosshead set the initial position of the crosshead. The crosshead was released by manually pulling out the locking pin. On the lower end of the guiderails, springs are included to cushion the fall of the crosshead. Two vertical aluminum rods connected the wedge impactor to the crosshead. In this setup, the accelerometer was attached to the top of the crosshead again using the sticky wax. The total mass of the moving part was 10 kg. The water basin below the drop test facility had the dimensions of 1.07 m in length, 1.11 m in height, and 0.10 m in width. It was aligned with the drop test facility such that the wedge impactor hit the water surface in its center. The water level was set to 0.68 m and regular tap water at room temperature was used as test liquid with a density of $\rho_w = 998\ \mathrm{kg/m^3}$.

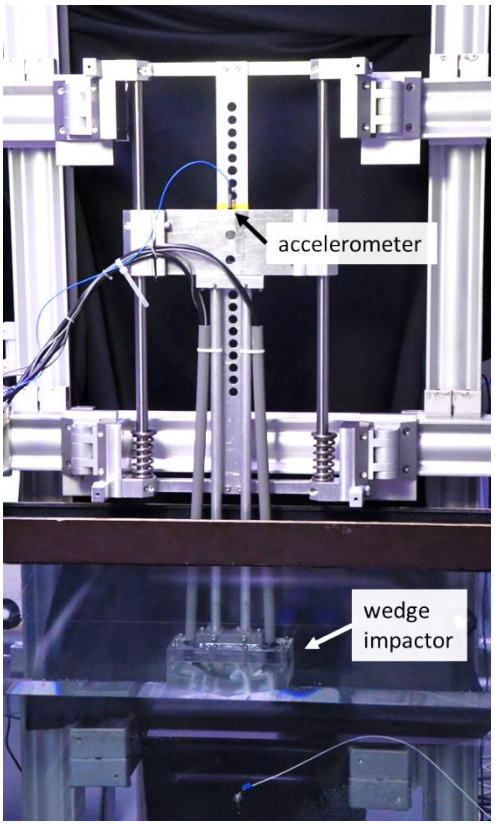

Fig. 5. Drop test facility with wedge impactor and accelerometer installed.

The high-speed camera recorded the impacts from the same side as the picture shown in Fig. 5. The camera pointed perpendicularly to the front pane of the water basin and its optical axis was aligned with the undisturbed water surface. The distance between the camera lens and the front of the wedge impactor was 1.3 m. With the known dimensions of the wedge impactor, the length scale of the camera images was calibrated to 7.5 px/mm in horizontal as well as vertical direction with an associated uncertainty of 2%.

Test Conditions

Hammer Test

In order to identify natural frequencies of the test setup for the wet drop test, a hammer test was carried out. In this test, the test setup was gently hit by a hammer at in total six different locations. These locations were the top of the crosshead, the top of the horizontal X95 profile between the lower supports of the guiderails, the outsides of the vertical side frame profiles left and right of the water basin, as well as the center of the front and back pane of the water basin, resp. Each location was hit three consecutive times and the test sequence was repeated for three different positions of the wedge impactor. Firstly, the wedge impactor was suspended in air with the crosshead resting on the locking pin. Secondly, the wedge impactor was submerged in the water basin, also with the crosshead resting on the locking pin. Thirdly, the wedge impactor was submerged with the crosshead resting on the cushioning springs. Note that the front and back pane were hit by hand instead of the hammer to prevent damage.

Wet Drop Test

The drop height h_0, measured between the apex of the wedge impactor and the undisturbed free water surface, was varied from 20 mm to 100 mm in steps of 20 mm. For each drop height, the impactor was dropped 6 times. Between two consecutive impacts, it was waited for the water surface to settle to rest again. Droplets, which had formed on the underside of the wedge impactor, were not removed between impacts. Due to the limited number of 8 data acquisition channels for the pressure sensors, two different sets of sensors were connected for 3 consecutive impacts. The summary of the test conditions and the pressure sensor configurations are presented in Tab. 2. Due to an electric malfunction, pressure sensor P06 could not be used. For continuous reference, pressure sensors P03 of the sensor arrays as well as the individual pressure sensors P11, P12, and P13 were connected for all impacts. The accelerometer was also used for all impacts. In total, 30 impacts were recorded.

Tab. 2. Overview of test conditions and pressure sensor configuration.

drop #	h_0/mm	P01	P02	P03	P04	P05	P06	P07	P08	P09	P10	P11	P12	P13
1,2,3	20	x	x	x	x	x						x	x	x
4,5,6	20	x		x				x		x	x	x	x	x
7,8,9	40			x				x	x	x	x	x	x	x
10,11,12	40	x	x	x	x	x						x	x	x
13,14,15	60	x	x	x	x	x						x	x	x
16,17,18	60			x				x	x	x	x	x	x	x
19,20,21	80			x				x	x	x	x	x	x	x
22,23,24	80	x	x	x	x	x						x	x	x
25,26,27	100	x	x	x	x	x						x	x	x
28,29,30	100			x				x	x	x	x	x	x	x

Impact Velocity and Reference Pressure

The theoretical impact velocity v_{0t} for a free-falling body in vacuum is given by Eq. (1) with drop height h_0 and gravitational acceleration $g = 9.81\ \mathrm{m/s^2}$.

$$v_{0t} = \sqrt{2g \cdot h_0} \tag{1}$$

Mainly due to friction, the actual impact velocity v_0 was expected to be lower than the theoretical value. Therefore, the actual impact velocity was determined from the images recorded by the high-speed video camera before and after the impact. This was done by measuring the pixel coordinates of the pixel corresponding to the apex of the wedge in the recorded frame and determining the displacement of the wedge over 10 consecutive frames, thus over a time interval of $\Delta t = \frac{1}{300}\,\mathrm{s}$. The pixel for

this measurement was determined manually. Therefore, the uncertainty of the distance was estimated as ± 2 px. Fig. 6 presents the frames selected from the recording of drop #01. The reference frame before the impact was chosen when the apex of the wedge had just penetrated the free water surface, marked with an arrow in frame #391. The reference frame after the impact was selected when the jet root had reached the chines of the wedge impactor, marked with the arrows in frame #450. The assessment of the impact velocity was carried out for 3 out of 6 drops per height. The results are summarized in Tab. 3. For the distances *s*, the overbar denotes the mean value and the indices 1 and 2 denote before and after impact, resp. Furthermore, the relative standard deviation of the measured distances $\sigma(s)/\bar{s}$ was calculated according to Eq. (2). As can be seen from Tab. 3, the difference between $\bar{s}_1$ and $\bar{s}_2$ fell within the uncertainty of the pixel measurement. Therefore, it was concluded that the change of velocity over the duration of the impact was negligible and the impact velocity was calculated from the total dataset obtained before and after impact.

$$\frac{\sigma(s)}{\bar{s}} = \frac{1}{\bar{s}} \cdot \sqrt{\frac{\sum_{i=1}^{n}(s_i - \bar{s})}{n-1}} \tag{2}$$

The reference pressure p_w for the peak pressures was calculated from Wagner's solution according to Eq. (3) (Wagner, 1932, Okada and Sumi, 2000) with β being the deadrise angle of the wedge w.r.t. to the undisturbed free water surface.

$$p_w = \frac{\rho_w}{2} v_0^2 \cdot \left(\frac{\pi}{2}\cot\beta\right)^2 \tag{3}$$

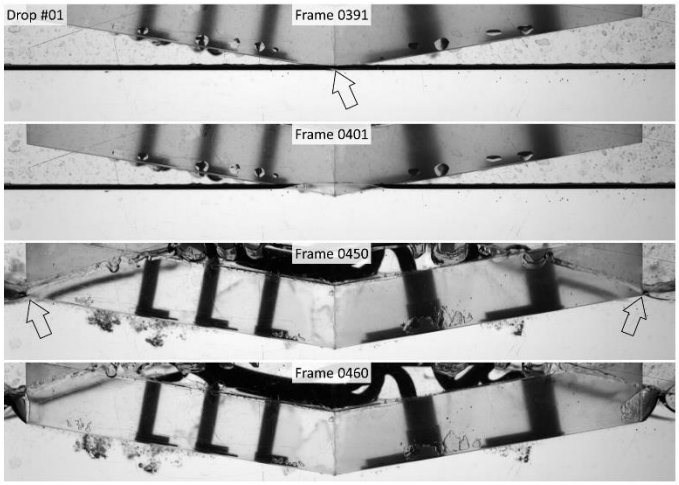

Fig. 6. High-speed video images of drop #01 used for velocity measurement. Frames #391 and #401 before impact; frames #450 and #460 after impact.

Data Processing

Data Preparations

For the dry acceleration test, data was recorded for 10 consecutive excitation runs in a single file. Using National Instruments DIAdem, this file was split up into 10 individual files for further processing, each file containing a single excitation run. Also using DIAdem, the data files of the hammer tests were visually inspected. The results for the three consecutive excitations per condition were reasonably similar. Therefore, only the first excitation and response per condition was further assessed.

Tab. 3. Impact velocities and reference pressure per drop height.

h_0/mm	20.0	40.0	60.0	80.0	100.0
v_{0t}/(m/s)	0.63	0.89	1.08	1.25	1.40
before impact					
$\bar{s}_1$/px	16.3	21.3	27.0	29.3	32.7
$\sigma(s_1)/\bar{s}_1$	3.5%	2.7%	3.7%	7.1%	1.8%
after impact					
$\bar{s}_2$/px	17.3	21.7	25.0	28.7	30.3
$\sigma(s_2)/\bar{s}_2$	3.3%	2.7%	0.0%	2.0%	1.9%
total					
$\bar{s}$/px	16.8	21.5	26.0	29.0	31.5
$\sigma(s)/\bar{s}$	4.5%	2.5%	4.9%	4.9%	4.4%
v_0/(m/s)	0.68	0.86	1.04	1.17	1.27
p_w/kPa	18.1	29.6	43.2	53.8	63.4

The main data processing was carried out using National Instruments LabVIEW software. The raw signals were recorded in mV/V for pressure channels and in Volts for accelerations. The first step was to determine the DC offset of all signals at the begin of each time series over a period of 0.2 s for the acceleration tests as well as over 2 s for the hammer and wet drop tests. The individual offset values were then subtracted from the time series data. Next, the first peak above a certain threshold in data channel P11 was detected to provide a time reference for the impact. The threshold was individually adjusted to ensure the correct peak was detected. For the reference time, the time instance when the rising flank of the signal reached 50% of the peak value was chosen. This reference time was marked as t_1 and its definition is presented in Fig. 7 using a generic signal.

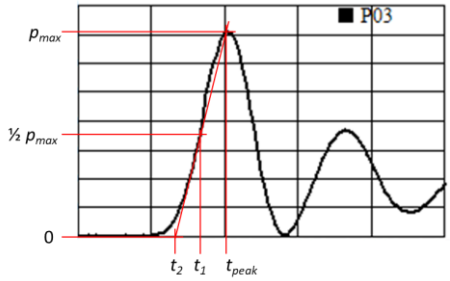

Fig. 7. Definition of peak pressure and time instances for data assessment.

Channel P11 was selected because this pressure sensor was located closest to the apex of the wedge impactor. Based on this reference time, standardized time series were extracted from the raw data. For the hammer test and the wet drop tests, these standardized series started 1.0 s before the reference time t_1 and had a duration of 3.0 s. For the wet drop tests, this duration was sufficiently long to cover the release of the locking pin of the drop test facility, the initial impact of the wedge impactor on the water surface, the following impact of the crosshead on the cushioning springs, and several rebounds. Further data assessment concentrated solely on first impact of the wedge impactor on the water surface. For the acceleration test, the series started 0.2 s before the reference time and covered a period of 0.7 s.

The standardized time series were then scaled from voltage information to the relevant physical quantities. For the accelerometer Acc and the pressure sensor Pxx the nominal calibrations factors were used. For pressure sensors P01 through P13, calibrations factors were determined from a calibration with static water head conducted before the wet drop tests.

Due to the lack of an input filter for the acceleration signal, the

acceleration signal was rather noisy. Therefore all signals were digitally low-pass filtered using a 3rd-order Butterworth filter with 20 kHz cut-off frequency and enforced zero phase shift. These filter settings were chosen to minimally affect the pressure signals and remove the noise from the acceleration signal. The scaled standardized time series of the unfiltered and filtered signals were stored in new data files. The filtered signals were identified by the extension "_flt" to the channel name.

For a first visual impression of the data obtained from the dry acceleration tests, two example time series for the unfiltered pressure and filtered acceleration signals are shown in Fig. 8. Note that the reference time was set to 0.2 s for these tests.

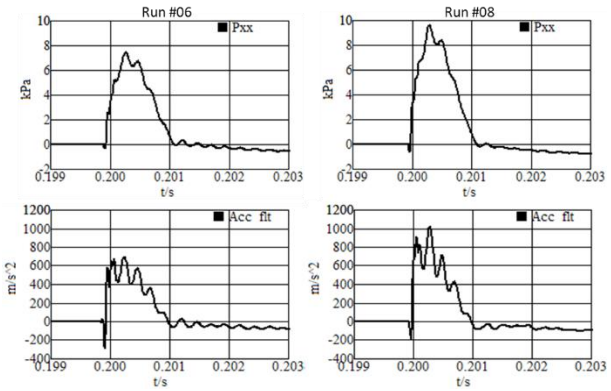

Fig. 8. Time series of pressure (top) and acceleration (bottom) signals from dry acceleration tests; left: run #06, right: run #08.

Fig. 9 presents an example for the pressure time series of a wet drop test, which are zoomed in on the initial impact. All pressure signals showed the distinct sharp rise in pressure with a consecutive peak and more gentle decay of the signal as expected for a drop test with a wedge. The last row of Fig. 9 shows the associated acceleration signal, unfiltered on the left and filtered on the right. Over the duration of the impact, an apparently linear rising trend could be observed in the acceleration signal, starting at around $a = -10\frac{\mathrm{m}}{\mathrm{s}^2}$ at $t = 0.998$ s and ending at approximately $a = 0\frac{\mathrm{m}}{\mathrm{s}^2}$ at $t = 1.010$ s.

Data Assessment

For the dry acceleration test, the peak values of the pressure and the filtered acceleration signals were determined using a built-in LabVIEW function. This LabVIEW function fitted a curve over 3 consecutive data points and determined the peak from the fitted parabola. Therefore, the identified peak pressure p_{max} and the peak acceleration a_{max} as well as the associated peak time t_{peak} did not necessarily coincide with one of the data points.

The hammer test was only assessed by visual inspection.

For the wet drop test, the peak pressures were identified in the same manner is described above. Furthermore, the difference Δt_{peak} in the peak time between any two pressure signals was calculated. The reference time t_1, see Fig. 7, was determined for all pressure signals. For this purpose, the LabVIEW function Transition Measurement was employed. This function detected when the signal crossed a predetermined threshold and determined the time of the crossing by linear interpolation between the two data points directly adjacent to the crossing. In this study, the threshold was set to 50% of the peak value of the peak subsequent to the flank.

The rise time t_{rise} of the impact pressure was determined by linear extrapolation according to Eq. (4), following the triangular approximation of the impact pressure as also proposed by Kim et al. (2015).

$$t_{rise} = t_{peak} - t_2 = 2\left(t_{peak} - t_1\right) \tag{4}$$

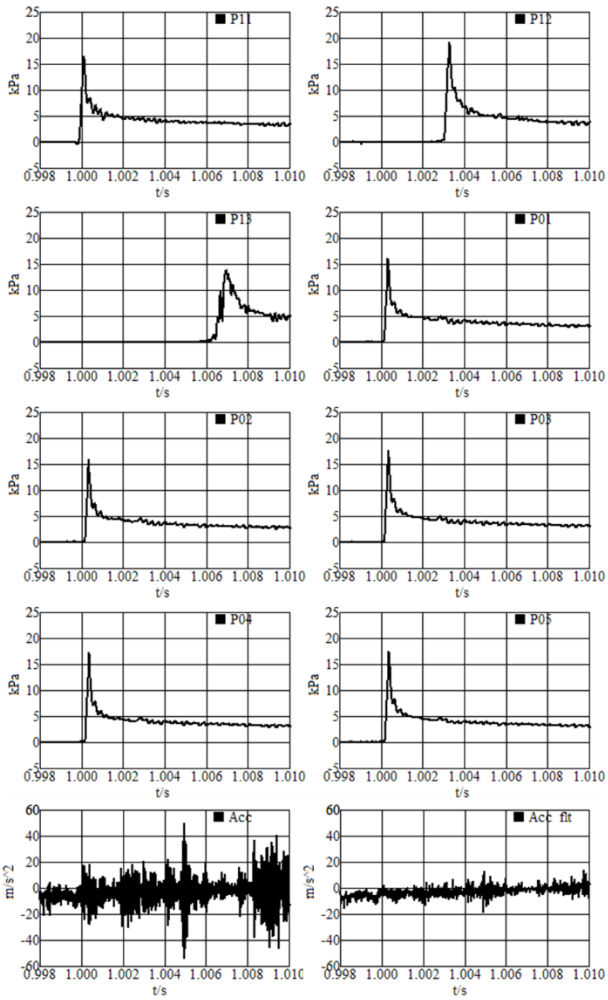

Fig. 9. Pressure and acceleration time series for drop #03, h_0 = 20 mm.

TEST RESULTS

Dry Acceleration Tests

A close-up of the pressure and acceleration signals of two representative runs of the dry acceleration tests are presented in Fig. 10. The total time covered by these graphs is 2 ms. In the bottom row, the acceleration signal of both started at zero with both pressure sensor and accelerometer at rest. The short dip and subsequent sharp rise of the accelerations over just fractions of milliseconds identified the tick given to the circuit board of the pressure sensor. The first peak around $t = 0.2000$ s includes some high-frequency oscillations with a frequency about 20 kHz, which coincides with the cut-off frequency of the applied filter. After the initial peak followed several secondary oscillation around the level of the first peak. These oscillations had a frequency of 4.8 kHz. After 0.5 ms, the acceleration began to decline and was back to a level of around 0 after a total impulse duration of 1 ms, with the secondary oscillations still visible in the signals.

The pressure signals in the top row started at a value of 0 and followed the general shape of the corresponding acceleration signal. On closer inspection, the rising flank of the pressure signals is less steep than the

acceleration signals, and the initial, high-frequency oscillations in the acceleration signals could only be traced as small steps in the pressure signals around $t = 0.2000$ s. Around the peak in the pressure signals, also secondary oscillations were identified with the same frequency of 4.8 kHz as in the acceleration signal. Also the pressure signals were back to their starting level after a total impulse duration of just over 1 ms.
When comparing the peak magnitude of pressure and acceleration signal, there was a difference of two orders of magnitude. The peak pressures were in the range of 7 to 10 kPa while the peak accelerations reached 700 to 1000 m/s^2.

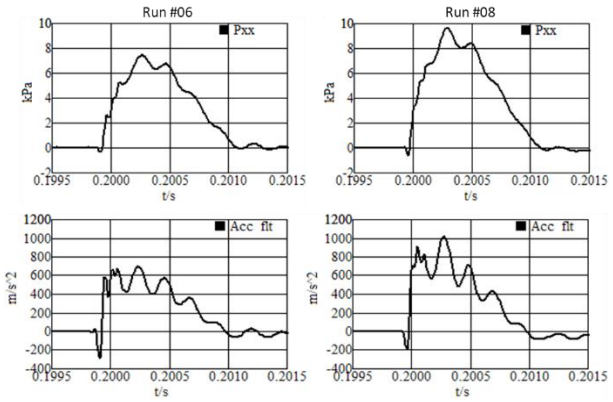

Fig. 10. Close-up of the pressure (top) and acceleration (bottom) signals from dry acceleration tests; left: run #06, right: run #08.

In order to assess the dependency between peak pressures p_{max} and peak accelerations a_{max}, these values were plotted against each other for all ten excitation runs. The resulting graph is shown in Fig. 11. There was a clear linear correlation between peak pressures and peak accelerations. The slope of the regression line indicated the sensitivity of the pressure sensors to acceleration, which was found to be 0.01 kPa/(m/s^2).

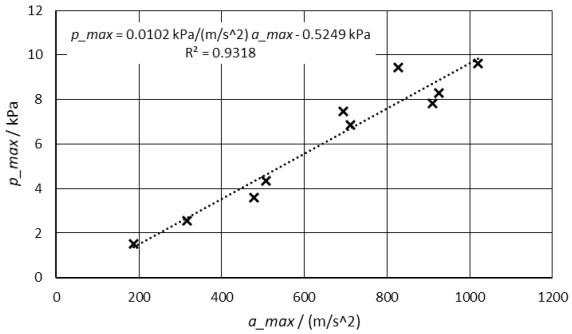

Fig. 11. Correlation between peak pressure p_{max} and peak acceleration a_{max} from the dry acceleration tests including linear regression line.

Wet Drop Tests

More results from the wet drop tests are shown in Figs. 12 and 13. These results were taken from drop #01 and drop #28 with the maximum and minimum drop height of h_0 = 20 mm and h_0 = 100 mm, resp. Please note the different scale on the pressure axis in the two figures. In both figures, the reference time of t_1 = 1.0 s can be seen for pressure sensor P11. Also the time difference between the impact at different sensor locations is clearly visible.

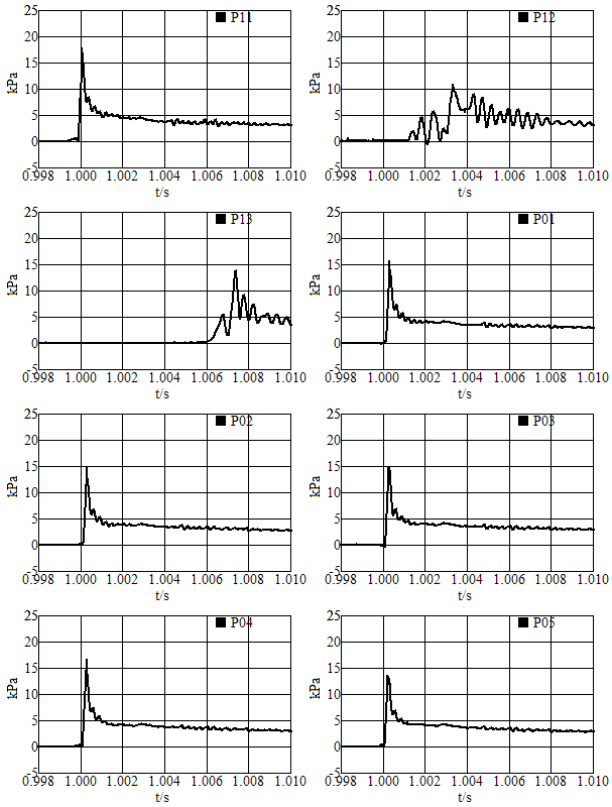

Fig. 12. Pressure time series for drop #01, h_0 = 20 mm.

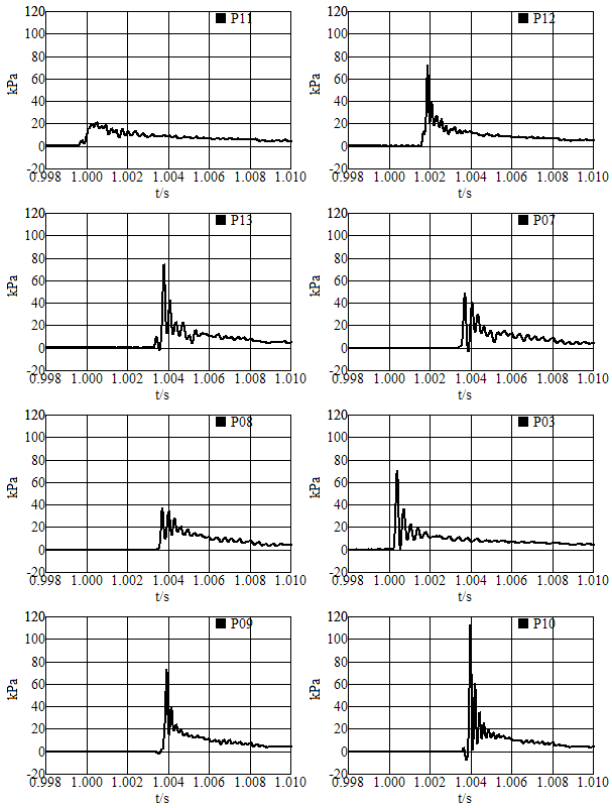

Fig. 13. Pressure time series for drop #28, h_0 = 100 mm

On closer inspection, the results from the wet drop tests confirmed that these tests, carried out with a wedge, created impact pressures with the

characteristic time trace of the jet root passing the sensor position (Kimmoun et al., 2016, Lafeber et al., 2012). In general, the impact pressures were reproducible in shape and magnitude. The comparison of signals within the individual drops as well as between the drops also revealed considerable variability between individual impacts. In drop #01, shown in Fig. 12, the sensors located on the left-hand side of the wedge impactor, i.e. P11, P12, and P13, produced clearly different pressure signals for the same impact. While P11 measured a sharp peak with fast decay of the pressure after the peak, the pressure signals from sensors P12 and P13 showed considerable oscillations with far less pronounced peaks. On the other side of the wedge impactor, the collocated pressure sensors P01 through P05 recorded almost identical pressure time series with a peak pressure around 15 kPa and smooth decay.
The pressure time series for drop #28 shown in Fig. 13 gave a similar result. Here pressure sensor P11 recorded a much smaller peak pressure of about 20 kPa as compared to the peak pressures of P12 and P13 between 60 kPa and 80 kPa. Also the remaining pressure signals of drop #28 varied more, with a wider distribution of peak pressures as well as varying levels of oscillations.

To investigate the cause of the variability, the high-speed video images of drops #01 (h_0 = 20 mm) and #28 (h_0 = 100 mm) were analyzed. Fig. 14 presents the image sequences of these drops covering the time from the apex reaching the free water surface until the chines got submerged. Within the individual sequence, the time step between images was kept constant. Note the different time step between the two sequences. In the left column, the lower part of the wedge impactor is clearly seen in the first two images. On the left side of the wedge impactor, some droplets of water were hanging below the sloping bottom plate at the location of sensors P12 and P13. On the right side of the impactor, there are no droplets visible on the bottom plate. Following the impact through the image sequence, clear water can be seen below sensors P11 and P01~P05, which were the sensors closest to the apex on the left and the right side, resp. Starting from frame #420, disturbances occurred in the water below sensor P12, and also below sensor P13 in frame #430. These disturbances were small bubbles and the location where those bubbles originated coincided with the location of the droplets before the impact. Without droplets on the bottom plate, only very small bubbles developed on the right side of the wedge impactor. This clearly correlated with the findings from the pressure signals in Fig. 12.
In the right column of Fig. 14, the image sequence of drop #28 revealed droplets hanging on both sides of the wedge impactor. As can be seen throughout the entire sequence, these droplets led to the generation of many bubbles over the entire bottom surface of the impactor. This corresponded to the larger variability of the pressure signals from this drop shown in Fig. 13. The effect of droplets increasing the variability of impact pressures was also reported by Neugebauer et al. (2017).

In order to assess the variability of the peak pressure, the values of the peak pressures were accumulated from all pressure sensors and all drops with the same drop height h_0. This provided 48 peak pressure values per drop height. For the comparison between the results from different drop heights, the peak pressures were normalized by the corresponding reference pressure p_w according to the Wagner solution given in Tab. 3. The resulting data is presented in Fig. 15, where the median value was plotted together with the minimum and maximum values as well as the high and low quartile values.
It is obvious from Fig. 15 that the spread of the normalized peak pressures was nearly the same for all drop heights, with the exception of the smallest drop height, which resulted in less spreading in the peak pressures. Despite the total range of $0.3 \leq p_{max}/p_w \leq 1.8$ of the normalized values was the median value within a $\pm 20\%$ interval around the reference pressure.

Fig. 14. Sequences of high-speed video pictures. Left: drop #01, $\Delta t = 1/300$ s between pictures; right: drop #28, $\Delta t = 1/600$ s between pictures.

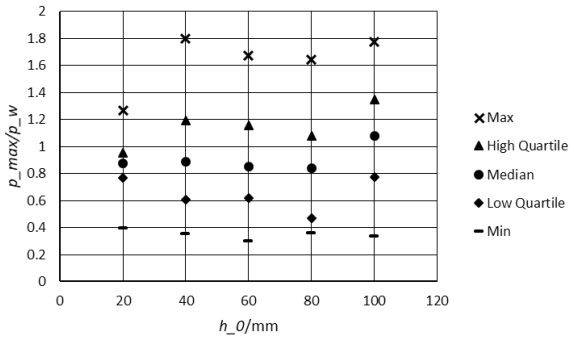

Fig. 15. Distribution of normalized peak pressures per drop height h_0.

The rise time t_{rise} of the pressure signals was assessed in a similar manner as the peak pressure. The data was accumulated over all pressure sensors per drop height and normalized by the reference time t_{ref} given by Eq. (5).

$$t_{ref} = \frac{d \sin \beta}{v_0} \tag{5}$$

If the free water surface is considered undisturbed by the entering wedge, this reference time t_{ref} represents the time required for the contact line between the water surface and the inclined bottom face to pass over the pressure port of the pressure sensors with the diameter $d = 0.4$ mm with the wedge falling at the velocity v_0. The values of t_{ref} are summarized in Tab. 4.

Tab. 4. Reference time per drop height.

h_0/mm	20.0	40.0	60.0	80.0	100.0
t_{ref}/s	1.03E-04	8.04E-05	6.65E-05	5.96E-05	5.49E-05

The resulting data was plotted in quartile steps in Fig. 16. This plot revealed that the lower 75% of the data was concentrated over a small range with the maxima being up to one order of magnitude larger than the median values. Therefore, the data was plotted again in Fig. 17 from

the minimum values up to the 90th percentile, which effectively excluded the 5 largest values.

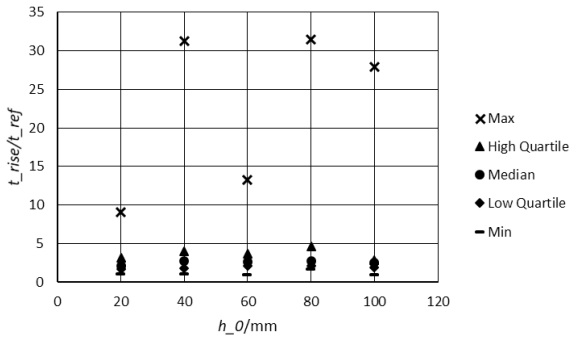

Fig. 16. Distribution of normalized rise time per drop height h_0.

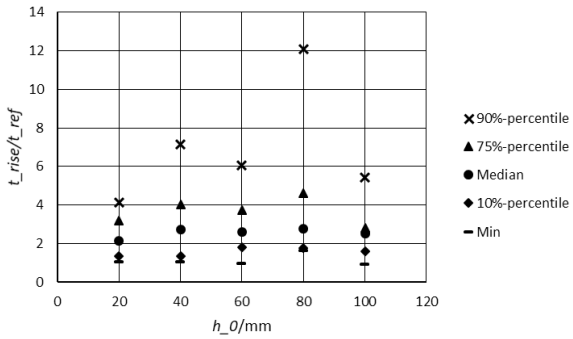

Fig. 17. Distribution of normalized rise time per drop height h_0, close-up up to 90th percentile.

Fig. 17 clearly showed that the median of the normalized rise time was in the range of 2 to 3, with the minimum around 1, independently of the drop height. Assume the pressure distribution in the root of the jet passing along the bottom face of the wedge is idealized as a step function at the location of the undisturbed waterline. Then the normalized rise time of $t_{rise}/t_{ref} = 1$ is the minimum value that can theoretically be expected. The slightly higher values of the normalized rise time confirmed that the actual pressure distribution had a steep but finite slope at the jet root. The absolute values of the median rise times were in the range of 0.15 ms to 0.25 ms.

After the global assessment of the wet drop test results, some pressure time series were inspected more closely. Fig. 18 shows the time series of sensor P03 from drop #03 together with the corresponding acceleration signal. The pressure signal exhibited the expected sharp rise to the peak of 17.5 kPa and initially an equally sharp decay, which gradually became more gently. Starting in the falling flank of the signal, pressure oscillations could be detected with a typical frequencies around 3.8 kHz. The acceleration signal in the right plot of Fig. 18 showed many high-frequency oscillations, even after filtering. Over the depicted time period of 4 ms, the average acceleration is about -5 m/s^2, with a slightly rising tendency. The amplitude of the high-frequency oscillations is between 5 m/s^2 and 10 m/s^2. Neither the sharp peak nor the aforementioned oscillations of the pressure signal could be traced back in the acceleration signal.

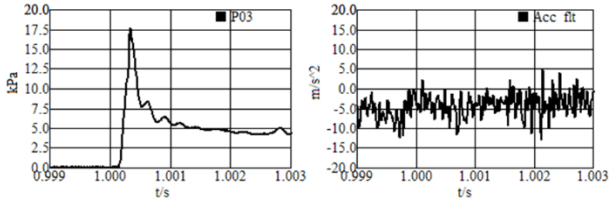

Fig. 18. Close-up on pressure time series of sensors P03 as well as acceleration for drop #03.

Fig. 19 shows the signals of pressure sensors P03 and P10 of drop #28 together with the corresponding acceleration signal. Both pressure sensors recorded pronounced pressure oscillations after the initial peak of 70 kPa and 110 kPa from sensors P03 and P10, resp. The frequencies of these oscillations were 2.8 kHz for sensor P03 and 4.6 kHz for sensor P10. Sensor P10 also measured a small oscillation in pressure before the highest peak.

The acceleration signal again revealed high-frequency oscillations with amplitudes of roughly 20 to 40 m/s^2 around a slowly rising mean value. The mean acceleration started at around 0 m/s^2 at t = 0.999 s and increased to about 20 m/s^2 at t = 1.007 s. The oscillations in the pressure signals could not directly be linked to features of the acceleration signal.

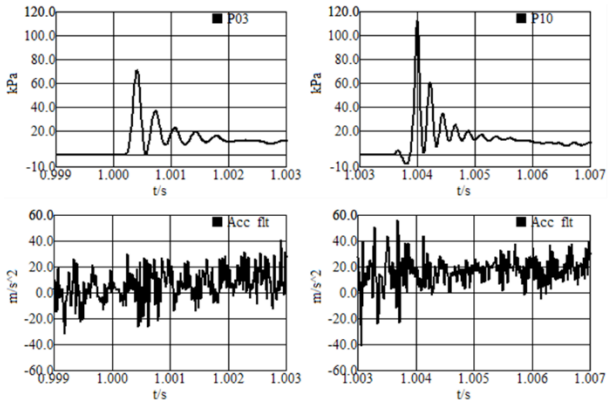

Fig. 19. Close-up on pressure time series of sensors P03 and P10 as well as acceleration for drop #28.

Hammer Tests

Selected results of the hammer test are presented in Fig. 20 for two different conditions, both with the crosshead resting on its locking pin and the excitation being provided by ticking the top of the crosshead. The time series presented in the left column of Fig. 20 were obtained with the wedge impactor being suspended in air. The data shown in the right column corresponded to the wedge impactor submerged in water. The top four rows show the signals from several pressure sensors while the bottom row presents the corresponding acceleration data.

Comparing the pressure and acceleration signals for both conditions, it was noted that there is a short delay of about 0.5 ms before the pressure signals started to oscillate after impact of the hammer was recorded by the accelerometer. Due to the distance between the accelerometer mounted on the crosshead and the pressure sensors in the wedge impactor, this delay was not further investigated.

All signals showed characteristic oscillations with frequencies around 3 kHz and the first oscillations of the pressure signals were in phase. With the excitation by the tick of a hammer, there was a clear link between the acceleration and the pressure signals. When looking at the amplitude of the acceleration signals, in both tests the first oscillations were in the order of 1000 m/s^2 to 2000 m/s^2. In the pressure signals, there

was a clear difference between the two tests. With the pressure sensors in air, the pressure signals reached levels between 1 kPa and 4 kPa, whereas when submerged in water, the sensors recorded oscillation amplitudes between 30 kPa and 50 kPa.

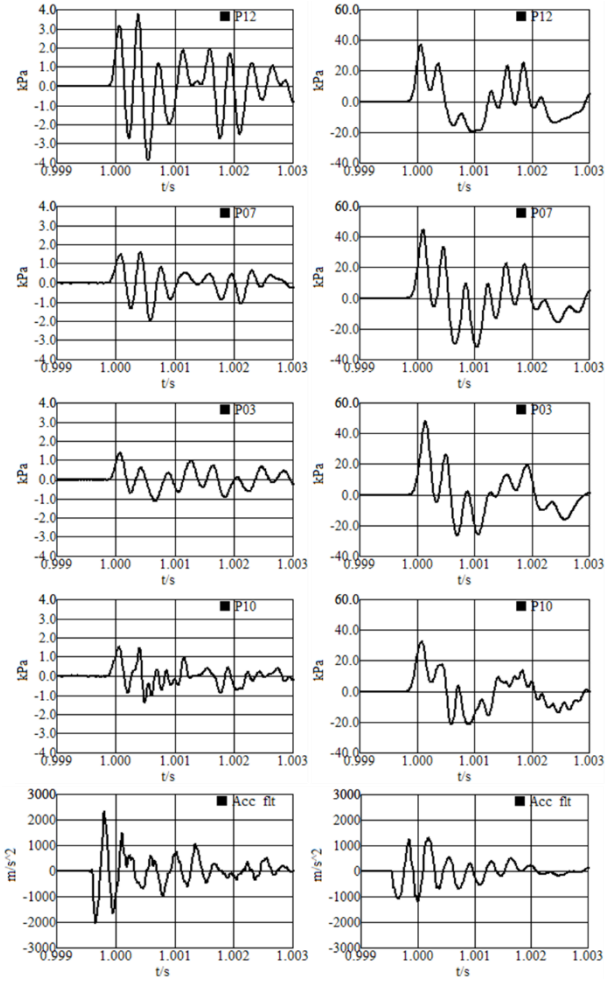

Fig. 20. Time series of hammer test. Left: wedge impactor in air, right: impactor submerged. Bottom row: acceleration

DISCUSSION

Sensitivity to Acceleration

Comparing the finding from the hammer test with the result of the dry acceleration test revealed that in air the pressure sensors measured only about 1/10 of the value, which could be expected based on the measured accelerations. On the other hand, in water the pressure values were higher than what would be predicted from the results of the dry acceleration tests by a factor of 3 to 4. Due to the different mounting conditions of the sensors in the dry acceleration test and in the wedge impactor, no direct conclusion could be drawn here. The reduced influence of acceleration on the pressure sensors in the impactor in air suggested that not the full acceleration measured at the crosshead was passed to the wedge impactor. This idea was supported by the delay between the acceleration and the pressure signal. In direct comparison of the pressure signals between the two conditions in Fig. 20, the amplitudes measured in water were larger by a factor of about 40. The obvious difference between the two conditions was the density of the medium in contact with the sensors. With the density ratio of water and air of about 800, the difference would be expected to be much larger. This requires further investigation.

The acceleration measured in the wet drop tests conducted in this study during the initial impact of the wedge were about two orders of magnitude less than during the hammer test and dry acceleration test. Therefore, it was concluded that the acceleration of the total wedge impactor had no significant influence on the measured pressure signals.

Wet Drop Tests

The results of the wet drop tests showed large variability, which was largely attributed to the droplets hanging on the bottom face of the wedge impactor prior to the impacts. Due to this variability, the results of the peak pressures and rise time were assessed in a statistical way by means of quartile plots. The median value of the peak pressure matched well with the values predicted based on Wagner's solution. Furthermore, the peak pressures generated in the wet drop tests covered the full measurement range of the sensors of 60 kPa above atmospheric pressure, with the highest values even exceeding this limit. All measured pressures were within the overload limit of the sensors of 250 kPa (absolute pressure) (EPCOS AG, 2009). All sensors survived the test.

For the rise time, Kim et al. (2015) found values mainly below 10 ms in their sloshing experiments. Furthermore, Razzak et al. (2013) recommended the rise time of a dynamic calibration device to be no more than 6 ms for sloshing experiments. The largest rise times found in the present study were between 0.9 ms and 1.5 ms. The median values were in the range of 0.15 ms to 0.25 ms, which was very close to the theoretical minimum of rise time for the impact pressures generated in this study. The shortest rise times were measured for the highest peak pressure values. Based on this finding, the specimen sensors proved to be highly dynamic in their response.

Overall Remarks

Since this study focused on dynamic response of the new pressure sensors, their long-term stability and reaction to thermal shock was not addressed here. The results shown by Schreier and Poelma (2018) indicated good long-term stability of the signal. Kim et al. (2015) reported on the sensitivity of various pressure sensors to thermal shock. In their study, the piezoresistive sensors showed little influence of sudden temperature change on the pressure signal. The results of the present study did not indicate strong influence of contact to the water, though dedicated experiments need to be conducted to quantify this effect.

CONCLUSIONS

In this study, we conducted dry acceleration tests and wet drop tests accompanied by a hammer test with very small pressure sensors to investigate their dynamic response and potential for use in sloshing experiments. From the assessment of the test results, the following conclusions were drawn.

- The pressure magnitude and rise time matched well with the values predicted by theory.
- Over the full measurement range, the pressure sensors showed a rise time below 0.25 ms, which was close to the theoretical minimum rise time of the generated impact pressures. Thus, the pressure sensors recorded the full dynamic of the impacts.
- The variability of the impact pressures was attributed to droplets on the bottom face of the wedge impactor. For future tests, these droplets should be removed between tests to improve repeatability and reduce the variation in test results.
- The dry acceleration test indicated low sensitivity of the pressure sensors to accelerations. The hammer test confirmed this finding in general, though more dedicated tests are deemed necessary to determine the actual sensitivity to accelerations.

In summary, the new small pressure sensors showed the required dynamic response to be applicable for sloshing model tests.
The next steps in the development are electrical, mechanical and thermal tests to further investigate the possible applications of these sensors.

ACKNOWLEDGEMENTS

The authors would like to thank Henk van Zeijl and his colleagues from the Else Kooi Lab of EEMCS Faculty, TU Delft for their competent support as well as the mounting and the wire-bonding of PSC sensors. Furthermore, the authors gratefully acknowledge the support of the technical staff of the Ship Hydromechanics Lab and the Fluid Mechanics Lab of 3mE Faculty, TU Delft.
This work is part of the public-private research programme Sloshing of Liquefied Natural Gas (SLING). The support by the Netherlands Organisation for Scientific Research (NWO) Domain Applied and Engineering Sciences, and project partners is gratefully acknowledged.

REFERENCES

Ahn, Y, Kim, KH, Kim, SY, Lee, SW, Kim, Y, and Lee, JH (2013). "Experimental Study on the Effects of Pressure Sensors and Time Window in Violent Sloshing Pressure Measurement," *Proc 23rd Int Offshore and Polar Eng Conf*, Anchorage, Alaska, USA, ISOPE, 3, 186-193.

Chuang, SL (1966). "Slamming of rigid wedge-shaped bodies with various deadrise angles", David Taylor Model Basin, Report No. 2268.

EPCOS AG (2009). "C32 Product Brief", http://www.texim-europe.com/promotion/449/pressure%20sensor%20c32_products%20brief_te.pdf, 05.03.2018.

Kim, KH, Choi, YM, and Hong, SY (2016). "Comparative Study on Pressure Sensors for 2D Wedge Drop", *Proc 26th Int Offshore and Polar Eng Conf*, Rhodes, Greece, ISOPE, 3, 7-13.

Kim, SY, Kim, KH, and Kim, Y (2015). "Comparative Study on Pressure Sensors for Sloshing Experiment", *Ocean Engineering* **94**, 199–212.

Kimmoun, O, Brosset, L, and Dupont, G (2016). "Experimental Study of Wave Impacts on a Corrugated Ceiling", *Proc 26th Int Offshore and Polar Eng Conf*, Rhodes, Greece, ISOPE, 3, 944-957.

Lafeber, W, Brosset, L, Bogaert, H (2012). "Elementary Loading Processes (ELP) involved in breaking wave impacts: findings from the Sloshel project", *Proc 22nd Int Offshore and Polar Eng Conf*, Rhodes, Greece, ISOPE, 3, 265-276.

Loysel, T, Chollet, S, Gervaise, E, Brosset, L, and De Seze, P-E (2012). "Results of the First Sloshing Model Test Benchmark," *Proc 22nd Int Offshore and Polar Eng Conf*, Rhodes, Greece, ISOPE, 3, 398-408.

Loysel, L, Gervaise, E, Moreau, S, and Brosset, L (2013). "Results of the 2012-2013 Sloshing Model Test Benchmark", *Proc 23rd Int Offshore and Polar Eng Conf*, Anchorage, Alaska, USA, ISOPE, 3, 141-152.

National Instruments Corp. (2010). "NI PXIe-4330/4331 Specifications", 375487C-01, ni.com.

Neugebauer, J, Liu, S, Potthoff, R, el Moctar, O (2017). „Investigation of the Motion Accuracy Influence on Sloshing Model Test Results ", *Proc 27th Int Offshore and Polar Eng Conf*, San Francisco, California, USA, ISOPE, 3, 1054-1061.

Nikfarjam, M, Yaakob, OB, Seif, MS, and Koto, J, (2017). "Investigation of Wedge Water-Entry Under Symmetric Impact Loads by Experimental Tests", *Latin American Journal of Solids and Structures*, dx.doi.org/10.1590/1679-78253315.

Okada, S and Sumi, Y (2000). "On the water impact and elastic response of a flat plate at small impact angles", *J Mar Sci Technol* **5,** 31–39.

PCB Piezotronics, (2011). ICP® Accelerometer Model 353B18, Spec Number 353-2160-80.

Razzak, S, Amaichan, J, Damion JP, and Sarraf, C (2013). "Dynamic Pressure Calibration", *Proc 23rd Int Offshore and Polar Eng Conf*, Anchorage, Alaska, USA, ISOPE, 3, 194-201.

Schreier, S, and Poelma, C (2018). "A New Generation of Sloshing Pressure Sensors", *Proc 28th Int Offshore and Polar Eng Conf*, Sapporo, Japan, ISOPE, 3, 788-793.

Shin, H, Seo, B, and Cho, SR (2018). "Experimental investigation of slamming impact acted on flat bottom bodies and cumulative damage", *Int J Naval Architecture and Ocean Engineering* **10**, 294-306.

Truong, T, Repalle, N, Pistani, F, Thiagarajan, K (2010). "An experimental study of slamming impact during forced water entry", *Proc 17th Australasian Fluid Mechanics Conference*, Auckland, New Zealand.

Wagner, H (1932). "Über Stoß- und Gleitvorgänge an der Oberfläche van Flüssigkeiten", *Zeitschr. f. Angewandte Mathematik und Mechanik* **12**(4), 193-215.